RSC Advances

PAPER

View Article Online
View Journal | View Issue

Cite this: *RSC Adv.*, 2024, **14**, 32802

Synthesis and characterization of novel uranyl clusters supported by bis(pyrazolyl) methane ligands: biomimetic catalytic oxidation, BSA protein interaction and cytotoxicity studies†

Nakul S.,[a] Bhagavathish R.,[a] Naveen V. Kulkarni, *[a] Ajeetkumar Patil, *[b] Suresh B. Arakera[c] and Sam John[d]

Received 2nd September 2024
Accepted 9th October 2024

DOI: 10.1039/d4ra06347c

rsc.li/rsc-advances

Two novel uranyl complexes were synthesized using bis-pyrazolyl methane ligands. The complexes were characterized by several spectroscopic techniques, including UV-Vis, IR, NMR, mass spectrometry, fluorescence, electrochemical, and thermogravimetric analysis. The solid-state structure of the complex **C1** was determined with the help of single-crystal X-ray diffraction studies. The complexes **C1** and **C2** efficiently catalyse the oxidation of 3,5-di-*tert*-butyl catechol and 2-aminophenol in the atmospheric air, imitating the catalytic activity of the catechol oxidase and phenoxazinone synthase enzymes. The kinetic parameters and the catalytic efficiency (K_{cat}/K_M) of the reactions were calculated. Formation of organic free radicals in the catalytic reactions was confirmed by EPR spectroscopy. The interaction of these complexes with the protein, bovine serum albumin, was investigated by using UV-Vis and fluorescence spectral analysis. The cytotoxicity of the complexes against MDAMB-231 and A549 cell lines was investigated, and IC_{50} values were determined.

Introduction

Depleted uranium, which is a major contributor to radioactive wastes, constitutes a critical environmental challenge in the present world.[1,2] Therefore, using its compounds in functional materials can have an impact on reducing environmental risk, creating a secure environment, and contributing to sustainability.

In recent years, there has been a surge in the synthesis and modeling of uranyl complexes due to their interesting structural diversities and unique coordination properties, making these complexes have potential applications in the fields of catalysis, photocatalysis, fluorescent materials, hydrogen evolution, gas storage, and sensing.[3–10] Significant advancements in the catalytic chemistry of uranyl complexes have occurred over the past 20 years. Uranyl complexes have the proclivity to display various oxidation stages varying from +2 to +6. UO_2^{n+} uranyl ions, where n can be 1 or 2, comprise the majority of the higher oxidation state of uranyl complexes. And UO_2^{2+} is the most prevalent form in the environment.[11]

Uranyl complexes play an important role in biochemistry because of their interaction with biological molecules. Uranyl salts, specifically nitrate and acetate, are commonly employed as contrast agents in electron microscopy.[12] Sulfadiazine-azo-azomethine dye-based uranyl complexes have demonstrated bactericidal activity against Gram-positive bacteria, as well as fungicidal action.[13,14] Across the years, Schiff base uranyl complexes have shown oncolytic,[15] antibacterial, and antifungal efficacy. These complexes show photoluminescence properties; thus, they can be used as spectroscopic markers or probes.[16] A wide range of proteins have been known to interact with the uranyl ion, which includes proteins associated with blood, bone growth, and intracellular proteins.[17,18]

Pyrazoles are a class of heterocyclic aromatic compounds known for their biological applications. Trofimenko pioneered the development of bis(pyrazolyl)alkane derivatives, which have now become a well-established category of stable bidentate ligands.[19] Bis(pyrazolyl)methane supported complexes have been explored in various fields including, in the development of antimicrobials,[20,21] catalysts for organic transformation

[a]*Department of Chemistry, Amrita Vishwa Vidyapeetham, Amritapuri, 690525, Kollam, Kerala, India. E-mail: naveenvkulkarni@am.amrita.edu*

[b]*Department of Atomic and Molecular Physics, Manipal Academy of Higher Education (MAHE), Manipal 576 104, Karnataka, India. E-mail: ajeetkumar.p@manipal.edu*

[c]*Department of Applied Genetics, Karnatak University, Pavate Nagar, Dharwad – 580003, Karnataka, India*

[d]*Research and Post Graduate Department of Chemistry, St. Berchmans College, Changanassery, Kottayam 686101, Kerala, India*

† Electronic supplementary information (ESI) available: ESI contains all the characterization data of the complexes such as IR, UV, NMR, Mass spectra and single crystal X-ray analysis; Spectral and kinetic data of the catechol oxidation reactions, aminophenol oxidation reactions, BSA-binding interactions are also provided along with the cytotoxicity analysis data. The XRD data of the complex **C1** is deposited in CCDC. CCDC 2329479. For ESI and crystallographic data in CIF or other electronic format see DOI: https://doi.org/10.1039/d4ra06347c

reactions,[22,23] and dye sensitized solar cells.[24] However, the coordination chemistry of bis(pyrazolyl)alkane ligands with uranyl ions has not been explored.

This work reports the synthesis and characterization of novel uranyl complexes supported by bis(pyrazolyl)methane ligands, and exploring their catalytic activity in the oxidation of catechol to quinone and oxidative dimerization of 2-amino phenol to 2-amino-phenoxazine-3-one. To the best of our knowledge, this is the first uranyl complex used for the oxidation of 2-amino-phenol. Also, this work investigates the interaction studies of the metal complex with BSA protein and the anti-cancer activity of the complex with the MTT lung cancer cells and MTT breast cancer cells.

Experimental

Synthesis of ligands

The preparation of the ligands, bis(pyrazolyl)methane (**L1**) and bis(3,5-dimethyl pyrazolyl)methane. (**L2**) (Fig. 1) was done according to the methods described in the literature.[20,25] Both the ligands were duly characterized using spectro-analytical techniques.

Synthesis of complexes

In a general procedure, 1.5 mmol of the ligand was dissolved in 5 mL of methanol and to which 1.5 mmol of uranyl acetate, dissolved in methanol (5 mL) was added with continuous stirring. The solution was stirred for a period of 2 h at room temperature. The solid product was obtained by slow evaporation of the solvent, which was washed with hexane and dried under air.

$[(L1)_2(UO_2)_4(H_2O)_2(OAc)_2]$ C1. Yield 92%; M.P. 196–200 °C; IR (KBr, selected, cm^{-1}) 3780 (m), 3330 (b), 3024 (m), 2923 (m), 2361 (w), 1550 (m), 1464 (m), 1338 (m), 1268 (s), 1144 (m), 1003 (m), 919 (s), 807 (s), 675.36 (s), 522 (s), 469 (w); UV-Vis (MeOH, 10^{-4} M) (λ in nm (Abs.) 205 (1.217), 222.5 (1.622), 262.5 (0.545)); ^{1}H NMR (DMSO-d_6, 500 MHz, 298 K, ppm) δ 7.94 (2H, b, 5-CHpz), 7.50 (2H, b, 3-CHpz), 6.39 (2H, s, CH_2), 6.28 (2H, b, 4-CHpz); $^{13}C\{^1H\}$ NMR (DMSO-d_6, 125 MHz, 298 K, ppm) δ 140.48 (3-CHpz), 131.02 (5-CHpz), 106.70 (4-CHpz), 64.65 (CH_2).

$[(L2)_2(UO_2)_4(H_2O)_2(OAc)_2]$ C2. Yield: 90%; M.P. 208–210 °C; IR (KBr, selected, cm^{-1}) 3330 (b), 3024 (m), 2923 (m), 2361 (w), 1550 (m), 1464 (m), 1338 (m), 1268 (s), 1144(m), 919 (s), 807 (s), 675 (s), 522 (m). UV-Vis (MeOH, 10^{-4} M) (λ in nm (Abs.) 220 (1.807), 265 (1.028)); ^{1}H NMR ($CDCl_3$, 500 MHz, 298 K, ppm) δ 6.03 (s, 2H, CHpz), 5.81 (s, 2H, –CH_2–), 2.40 (s, 3H, CH_3 pz), 2.06 (s, 3H, CH_3 pz); $^{13}C\{^1H\}$ NMR ($CDCl_3$, 125 MHz, 298 K, ppm) δ 147.51 (pz(3)-CCH_3), 140.44 (pz(5)-CCH_3), 106.0 (pz(4)-CH), 59.29 (pz-CH_2-pz), 13.78 (pz(3)-CCH_3), 11.19 (pz(5)-CCH_3).

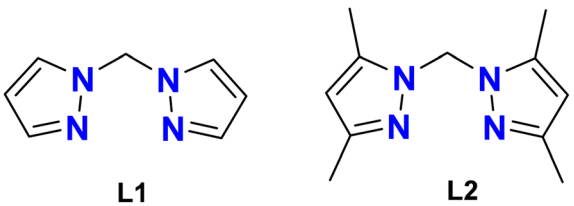

Fig. 1 Structure of ligands, L1 (bis(pyrazolyl)methane) and L2 (bis(3,5-dimethyl pyrazolyl)methane).

X-ray crystal studies

Single crystal X-ray analysis of complex **C1** was performed using a yellow, block-shaped crystal (size – 0.29 × 0.12 × 0.07 mm^3). A Bruker D8 Quest apparatus was used to obtain the diffraction data at 300 K. For the analysis, SADABS multi-scan absorption correction technique was used and data integration was done by using SAINT. Bruker SHELXTL package was used to solve and refine the structure.[26,27] Non-hydrogen atoms were represented anisotropically and hydrogen atoms were treated isotropically using a riding model (HFIX 43) at predefined places. The images and data provided in this article were produced by the WinGX suit[28] and Mercury.[29] Details of the crystallographic data are provided in ESI.†

Catecholase activity and kinetic studies

A well-known model compound, 3,5-di-*tert*-butylcatechol (DTBC) was used as the substrate to investigate the catecholase activity of the uranyl complexes. Using a UV-Vis spectrophotometer, the conversion of the substrate (DTBC) to the oxidised species 3,5-di-*tert*-butyl benzoquinone (DTBQ) was monitored at 400 nm over the course of 120 minutes at room temperature, in methanol, with observations made every 10 minutes. The catalyst-to-substrate ratio for the reaction was set to be 1 : 100 (0.1 mmol : 10 mmol). Further, the reaction parameters, *i.e.*, solvent, pH, temperature, *etc.* were varied to achieve the optimum catalytic activity. The kinetic studies were conducted and the kinetic parameters such V_{max}, K_M and K_{cat} were calculated from Michaelis Menten equation plot and Lineweaver Burk plot.[30,31]

Phenoxazinone synthase-like activity and kinetic studies

The metal complexes were utilized to perform the phenoxazinone synthase activity, with 2-amino phenol serving as the model substrate. The reactions were carried out at ambient temperature under aerobic conditions, utilizing water: methanol mixture (1 : 1) as the solvent. Various catalyst-to-substrate ratios such as 1 : 50, 1 : 100, 1 : 200 and 1 : 500 were tested to determine the catalyst's effectiveness. To understand the effects of solvents on the activity of phenoxazinone synthase, we conducted a reaction using various solvents, including water methanol and DMSO. The reactions were monitored and analysed using spectrophotometer analysis. The progress of the reaction was tracked by observing an increase in the distinct absorption peak of the resulting compound, 2-amino-phenoxazine-3-one, at a wavelength of 425 nm over a duration of 2 hours. The analysis was conducted at 10 minute intervals. The rate of the reactions was calculated using the initial slope of the plot of absorbance *vs.* time. We determined the T_∞ value to calculate the rate in terms of concentration. To understand the effect of substrate concentration on the rate of the reactions, a Michaelis Menten plot was constructed and various kinetic parameters were calculated using Lineweaver Burk Plot.[30,32]

Detection of hydrogen peroxide in the oxidation of DTBC

The catalytic mixture was prepared in 1 : 10 (catalyst : substrate) ratio in methanol (10 mL). After 2 h of reaction the reaction mixture was mixed with water (10 mL) and extracted using dichloromethane. The aqueous layer was acidified with 0.1 M H_2SO_4 and maintained a pH of ~2. 1 mL of 10% KI was added to the acidified solution, followed by 2–3 drops of 3% ammonium molybdate. The solution turns bluish black and the formation of I_3^- was detected using a UV-Vis spectrophotometer.

In vitro cytotoxicity studies

Cytotoxicity assessment (MTT Assay). The impact of complexes **C1** and **C2** on the MDA-MB-231 (Breast Cancer cell) and A549 (Lung Cancer Cell) cell lines was assessed by the conventional colorimetric MTT assay. The cell cultures were trypsinized and the cell count was modified to approximately 10 000 cells using DMEM (Dulbecco's Modified Eagle Medium). 200 μL of the cell suspension were added to each well of the 96 well microtiter plate. The plate was then incubated at 37 °C and 5% CO_2 atmosphere for 24 hours. The cells were exposed to the complexes for 24 hours in a medium containing metal complex concentration ranging from 10 to 50 μg mL^{-1}. The plate was removed from the incubator and the drug containing media was aspirated. 100 μL of medium containing 10% MTT reagent was then added to each well to get a final concentration of 0.5 mg mL^{-1} and the plate was incubated at 37 °C and 5% CO_2 atmosphere for 3 h The culture medium was removed completely without disturbing the crystals formed. Then 100 μl of solubilisation solution (DMSO) was added and the plate was gently shaken in a rotary shaker to solubilize the formed formazan. The absorbance was quantified using a microplate reader at two specific wavelengths: 570 nm and 630 nm. The percentage growth inhibition was determined by subtracting the background and blank values. The cytotoxicity has been assessed using the MTT assay, with cancer cells treated with cisplatin as a positive control and untreated cancer cell as the negative control under similar conditions. The results of the cytotoxicity activities on the cell lines against the metal complexes were evaluated with the dose value of the metal complex required to reduce the cell lines to 50% (IC_{50}).[33–36]

Result and discussion

IR and Raman spectral studies

In the IR spectrum of **C1**, the pyrazole ring ν(C–H) vibrations are seen as medium to strong intensity bands at 3025 cm^{-1}. Pyrazole ring ν(C=N) vibrations are responsible for the broad bands observed at 1515 cm^{-1} and 1399 cm^{-1}. The strong, intense band seen at 1470 cm^{-1} and the medium band observed at 1275 cm^{-1} are attributed to the C=C and C–N vibrations of the pyrazole ring, respectively. In the range of 1092 cm^{-1} to 1024 cm^{-1}, the strong bands observed are attributed to ν(N–N) vibrations. ν(O–H) stretching is attributed to prominent, intense bands observed at 3346 cm^{-1} and 3124 cm^{-1}, which denote the presence of water molecules.[24,37] Strong bands observed between 900 to 940 cm^{-1} are assigned to uranyl asymmetric normal vibrations.[38] The strong absorption observed at 691 cm^{-1} results from the acetate groups attached to the uranyl group by covalent bonds. Similarly, in the IR spectrum of **C2**, pyrazole ring ν(C–H) and methyl ν(C–H) vibrations are observed as medium intensity bands at 3024 cm^{-1} and 2923 cm^{-1} respectively. A strong band observed at 1550 cm^{-1} is attributed to pyrazole ring ν(C=N) vibrations. An intense band observed at 1464 cm^{-1} is assigned to vibrations of pyrazole ring ν(C=C). Medium intense bands observed at 1268 cm^{-1} and 1003 cm^{-1} correspond to the characteristic pyrazole ring group vibrations ν(C–N) and ν(N–N). A strong band observed at 3330 cm^{-1} is assigned to O–H stretching, indicating the presence of water molecules. The strong peak at 919 cm^{-1} is due to the anti-symmetrical normal vibration of the uranyl ion.[39] The strong absorption at 675 cm^{-1} results from the acetate groups attached to the uranyl centre. The IR spectra of the ligands (**L1** and **L2**) and complexes (**C1** and **C2**) are provided in the ESI.† The Raman spectra of the complexes **C1** and **C2** were analysed. A medium intensity peak observed at 842 cm^{-1} in **C2** corresponds to the U=O stretching vibrations.[40] In the case of **C1**, it is observed as a weak peak. The broad peak observed in the range of 100–300 cm^{-1} for both the complexes is attributed to combination of uranyl bending vibrations.[41] The U–N stretching vibrations are expected to appear in the region below 200 cm^{-1} as weak-bonds are perhaps masked under this broad peak. Other prominent peaks observed around 1500 cm^{-1} are originating from ligand C=C and C=N vibrations.[42] Raman spectra of both the complexes are provided in the ESI.†

Photophysical properties

The photophysical properties of the complexes (**C1** and **C2**) were analysed using UV-Vis, NIR and photoluminescence (PL) spectroscopy in MeOH at 10^{-3} M concentration and compared with the precursor uranyl acetate.

In the absorption spectra of the complexes **C1** and **C2**, absorption bands observed at around 220 nm and 265 nm are assigned to $\pi \rightarrow \pi^*$ and $n \rightarrow \pi^*$ transitions respectively. Both the complexes **C1** and **C2** exhibit a slight shift in absorption wavelength in comparison to their respective ligands,

Table 1 Optical properties of the compounds C1 and C2

Compounds	Absorbance λ_{max} solution (nm)	Emission λ_{max} solution (nm)	Optical bandgap (direct) E_g (eV)	CIE coordinates
C1	220, 265	403	5.21, 3.95	0.154, 0.259
C2	222, 265	403	5.13	0.155, 0.265

demonstrating the involvement of pyrazole ring azomethine groups in the coordination.[43] Using the UV-visible spectral data, with the help of Tauc plot, the direct optical band gap (E_g) of the complexes **C1** and **C2** were calculated[25] and are listed in Table 1. In the NIR spectra of the **C1** and **C2**, weak absorption peaks observed in the range 1000–1500 cm^{-1} are ascribed to f–f transitions of uranium.[44] The UV-visible and NIR spectra of ligands (**L1** and **L2**) and complexes (**C1** and **C2**) and the corresponding Tauc plots used for the calculation of direct band gaps are provided in ESI.†

In the emission spectra, the metal complexes **C1** and **C2** showed slightly increased intensity values for the emission peak as compared to the bare uranyl acetate (Fig. 2), however, no observable shift in the wavelength was observed. This increased intensity can be attributed to the increased electron density on the metal due to ligand coordination.[45] It was evident that, complex **C2**, which contains electron donating group on the pyrazole ring, exhibited slightly higher intensity as compared to **C1**.[46] The emission intensity values were plotted on the CIE 1976 (Commission Internationale deL'Eclairage) and represented in Fig. 3 and the CIE coordinates are listed in Table 1.

NMR studies

The H^1 NMR spectrum of the uranyl complex **C1** was compared with the ligand **L1**.[24,25] Same four peaks were observed as those of the ligand, however, with a slight variation in the chemical shift values owing to the metal chelation. The triplet observed at 6.28 ppm is attributed to the protons of the pyrazole ring, and a singlet at 6.39 ppm is due to the methylene protons. The signals due to other protons of the pyrazole ring are observed at 7.49 and 7.94 ppm. In the corresponding $^{13}C\{^1H\}$ NMR of the complex, four signals were observed. Three pyrazole ring carbons were observed at 106.70, 131.02 and 140.48 ppm and a peak at 64.60 ppm was ascribed to the methylene carbon. Similarly, in the H^1 NMR of the complex **C2**, a slight change in the chemical shift values is observed as compared to ligand.[20] The peaks at 2.06 and 2.40 ppm correspond to the methyl group present in the 3rd and 5th position of the pyrazole ring, while the methylene protons are observed at 5.81 ppm. The pyrazole ring proton was observed at 6.03 ppm. In the corresponding $^{13}C\{^1H\}$ NMR spectrum, the peaks observed at 11.19 and 13.78 ppm correspond to the methyl group carbons. Pyrazole ring carbons (3 & 5-pz) are observed at 141.0 ppm. Methylene linker and pyrazole ring (4-position) carbon signals are seen at 57.3 and 106.2 ppm, respectively.[20,25]

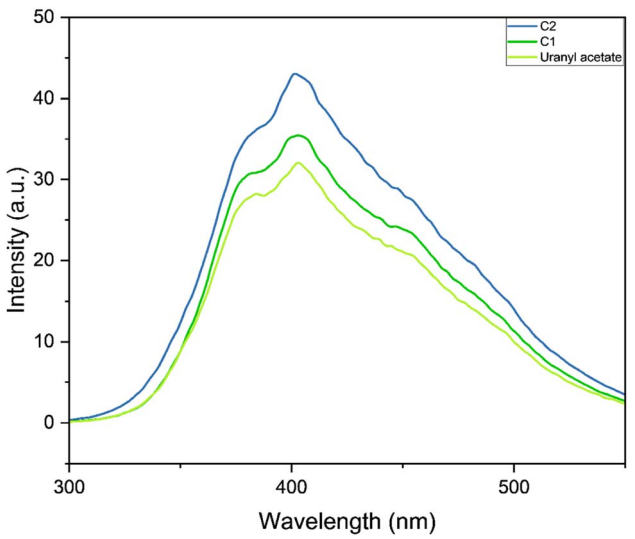

Fig. 2 Emission spectra of the complexes **C1**, **C2** and uranyl acetate.

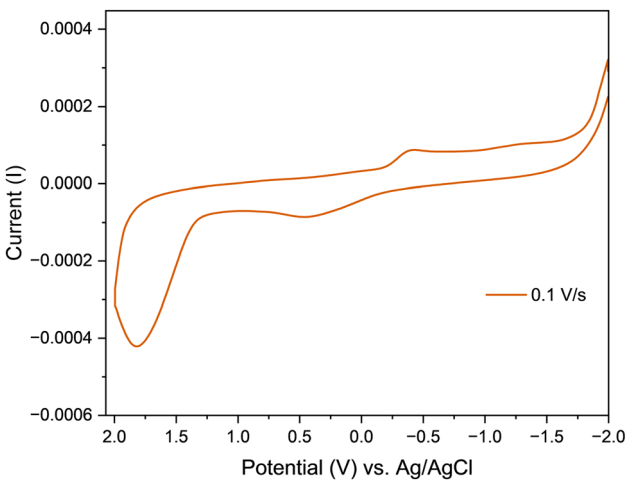

Fig. 4 Cyclic voltammograms of complex **C1** at different scan rates.

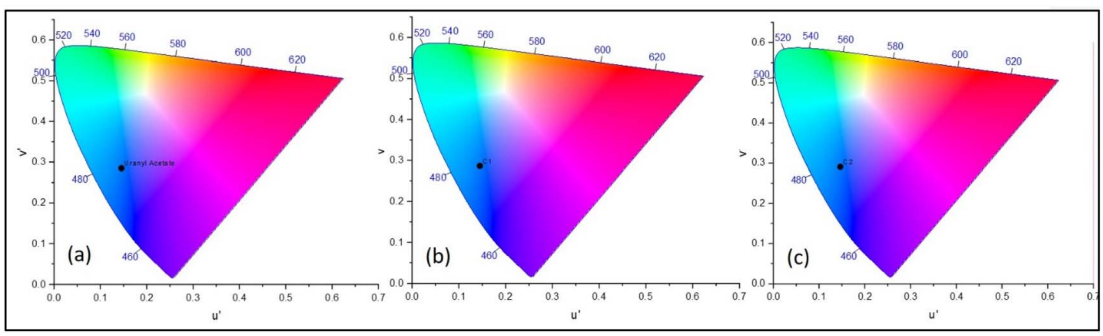

Fig. 3 CIE chromaticity diagram for (a) uranyl acetate. (b) Complex **C1** and (c) complex **C2**.

Mass analysis

Mass analysis of both the complexes, **C1** and **C2** was performed. In the mass spectrum of complex **C1**, the peaks of high intensity observed at *m*/*z* 886.20, 841.23, 797.22, 651.18, 607.17, 563.18, 454.10 and 417.12 indicate the fragmentation of the uranyl complex cluster in the mass analysis experimental conditions. Similarly, complex **C2**, exhibited high intensity peaks at *m*/*z* 943.34, 753.27, 709.26, 665.24, 519.19 and 475.18. The mass spectra of both the complexes are provided in ESI.†

Electrochemical studies

Complex **C1** was subjected to a room-temperature cyclic voltammetry analysis using three electrode system with a platinum counter electrode, a glassy carbon working electrode, and an aqueous Ag^{+}/AgCl reference electrode (0.1 M). KCl solution was used as a supporting electrolyte. These studies were carried out in water in the potential window run from −2.0 V to 2.0 V, at the scan rate of 0.1 V s^{-1}. Only the complex **C1** was found to exhibit redox activity, it displayed a cathodic peak at −0.405 V and an anodic peak at 0.425 V (Fig. 4). This quasi-reversible redox process was attributed to the reduction of the uranyl ion *i.e.*, $UO_2^{2+} + e^- \rightarrow UO_2^{+}$ and the corresponding oxidation reaction *i.e.*, $UO_2^{+} \rightarrow UO_2^{2+} + e^-$ respectively.[47]

X-ray crystal structure

The unit cell of complex **C1** is in a monoclinic crystal system and has a space group of $P2_1/c$. The complex contains a cluster of four uranyl centres mutually connected by four bridging oxygens and two bridging acetate ligands. All the four uranyl centres are found to have distorted pentagonal bipyramidal geometry,[48] with two perpendicularly placed oxo ligands, one bridging oxygen and one oxygen from acetate group taking the four coordination positions. For the two uranyl centres, the bidentate bis(pyrazolyl)methane ligands and a bridging oxygen take the remaining three positions and for the other two uranyl centres, two bridging oxygens and coordinating water molecule occupy the three coordination positions (Fig. 5). The average U=O bond length is found to be 1.78 Å and the average U–O bond length with the bridging oxygen is found to be 2.30 Å. The average U–O bond length with acetate oxygen is found to be 2.37 Å. These bond length values are in accordance with previously reported values.[49] All the important bond lengths and angles are provided in the ESI.† Interestingly, free ligand molecules (*i.e.*,

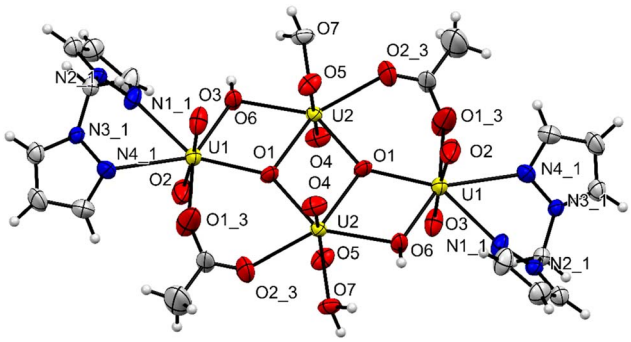

Fig. 5 The molecular structure of the uranyl cluster complex **C1** with 50% probability ellipsoids. Bond lengths and angles and provided in ESI.†

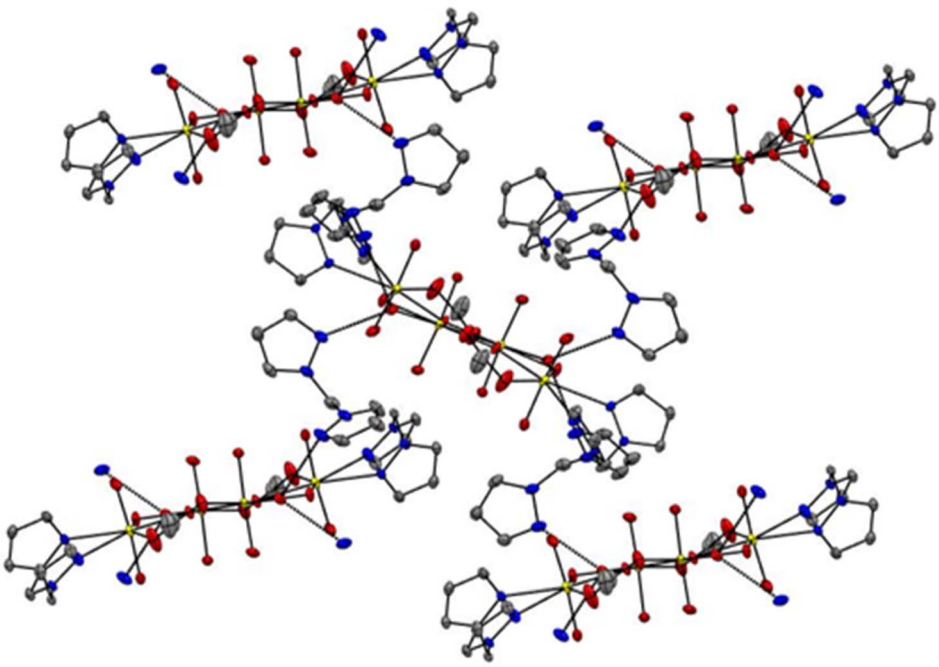

Fig. 6 3D network generated by the hydrogen bonding interaction between uranyl cluster and free ligand, bis(pyrazolyl)methane, in complex **C1** (colour code: yellow – uranium, red – oxygen, blue – nitrogen, and grey – carbon; hydrogen bonds are indicated as dotted lines, average bond length ~2.8 Å).

bis(pyrazolyl)methane) were seen to strongly interact with the uranyl clusters *via* hydrogen bonding (average bond length ~2.80 Å) with coordinated water molecules and form a three-dimensional network (Fig. 6).

Powder X-ray diffraction studies

Powder X-ray diffraction patterns are obtained for the **C1** (Fig. 7a) and **C2** (Fig. 7c) complexes. The PXRD data of the complex **C1** was compared with the PXRD pattern generated (Mercury software) from Single Crystal XRD data of **C1** (Fig. 7b). The prominent PXRD peaks of the **C1** were found to match well with the generated pattern indicating their similar structure. On the other hand, the complex **C2** exhibited distinct and narrow peaks indicating the high degree of crystallinity. We calculated the crystalline sizes for **C1** and **C2** using Debye–Scherrer formula[50] and values were found to be 43 nm and 41 nm, respectively.

Thermogravimetric analysis

The thermal gravimetric analysis was conducted for the complexes **C1** and **C2** using a heating rate of 10 °C min^{-1}. The complex **C1** decomposes in different steps as the temperature increases. Initially, the complex **C1** experiences a mass loss in the temperature range of 100–180 °C due to the removal of coordinated water molecules from the metal complex. In the second stage, mass loss occurs in the temperature range of 200–350 °C due to the decomposition of ligand. Finally, a stable mass was reached at high temperatures corresponding to the formation of uranyl trioxide.[50] For the complex **C2**, initially there was a loss of water molecules from the complex in a temperature range of 50 to 90 °C. The organic molecule elimination within a temperature range of 100 to 400 °C causes a mass loss in the second phase. The stable mass corresponding to UO_3 was obtained in a temperature range of 400 to 460 °C.[50,51] Corresponding thermograms are provided in ESI.†

Catecholase activity

The most widely used model compound, 3,5-di-*tert*-butyl catechol (DTBC) was utilised as the catechol substrate in the current studies.[31] The catalytic reactions were performed under various conditions and meticulously monitored by UV-Vis spectroscopy. To analyse the formation of the oxidation product, 3,5-di-*tert*-butyl benzoquinone (DTBQ), an increase in the absorbance at 380 nm was tracked. A slight shift in the peak from the usual value, 400 nm is likely the result of the catalyst and substrate interaction.[52] The preliminary studies were carried out at room temperature with neutral pH in methanol solvent under air. The UV-visible spectrum of the reaction was measured every 10 minute for 2 hours. Further reaction conditions were varied

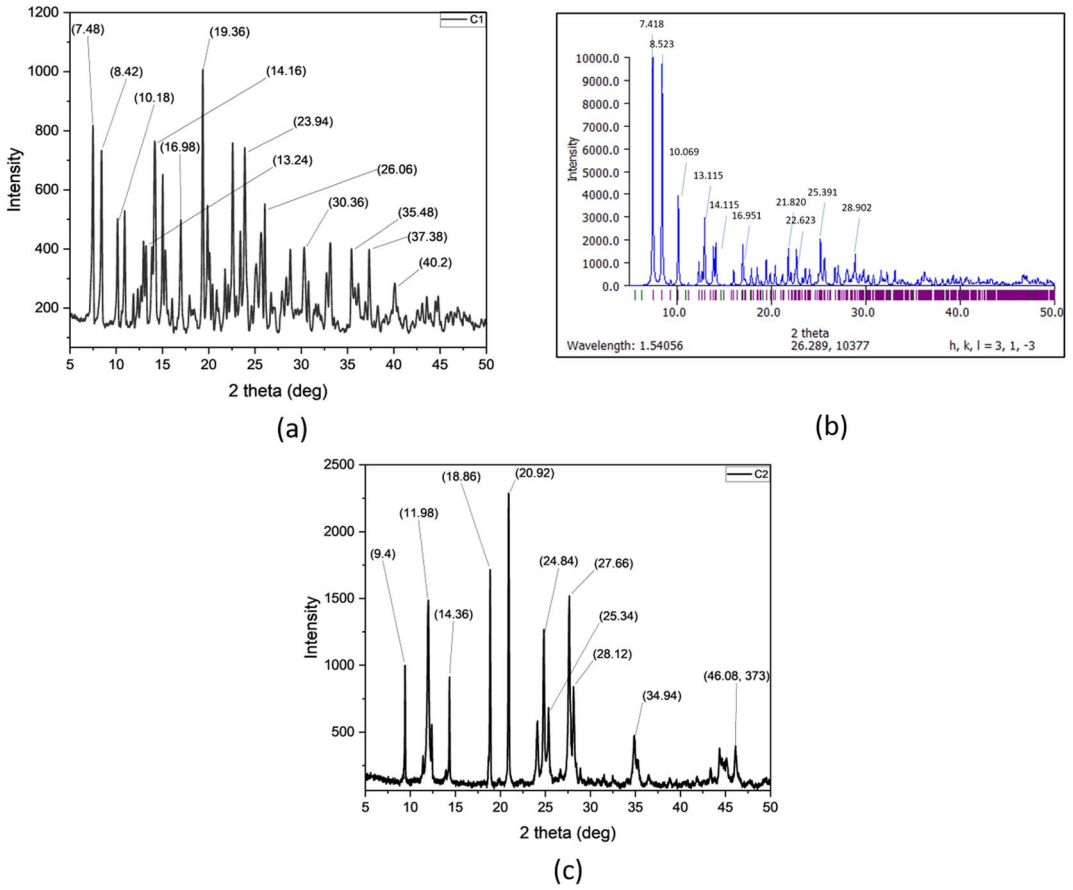

Fig. 7 (a) PXRD pattern of complex **C1**, (b) PXRD pattern of complex **C1** generated from Mercury software. (c) PXRD pattern of complex **C2**.

Table 2 Average rate of catalytic reactions (catalyst : substrate (1 : 100)) determined with the help of UV-visible spectral analysis

Sl. no.	Condition	Solvent	Catalyst used	Average rate (M min^{-1})
1	25 °C, pH 7.2	MeOH	**C1**	1.10×10^{-5}
2	25 °C, pH 7.2	MeOH	**C2**	1.11×10^{-5}
	25 °C, pH 7.2	DMSO	**C1**	0.014×10^{-5}
4	25 °C, pH 7.2	MeOH : water (1 : 1)	**C1**	0.80×10^{-5}
5	25 °C, pH 10	MeOH	**C1**	1.11×10^{-5}
6	25 °C, pH 3	MeOH	**C1**	0.42×10^{-5}
7	50 °C, pH 7.2	MeOH	**C1**	1.92×10^{-5}
8	25 °C, O_2 purged, pH 7.2	MeOH	**C1**	1.28×10^{-5}
9	25 °C, pH 7.2	MeOH	Uranyl acetate	0.52×10^{-5}

with respect to solvent, pH and temperature to see their impact. Every catalytic reaction was run for at least two times and the reaction rate was calculated using initial slope of ΔA *vs.* time plots and concentration (M) *vs.* time graph.[9,31,53] The average rate values are provided in the Table 2. Both complexes **C1** and **C2**, exhibited similar reactivity, displaying very good catechol oxidase mimicking property of the complexes (Entry 1 & 2, Table 2). This catalytic activity was found to be almost double as compared to the bare uranyl acetate under same reaction conditions (Entry 9, Table 2). Since both the complexes exhibited comparable activity, we proceeded with complex **C1** for further investigations. To examine the effect of solvent on the oxidation reaction, the reaction media was changed to different solvents, using DMSO (Entry 3, Table 2), lead into diminished reactivity, while a mixture of methanol and water (1 : 1) (Entry 4, Table 2) resulted into a slight decrease in the activity. It was evident that, the solvent plays a prominent role in the catecholase activity and methanol is the most appropriate solvent for this system.[54] Higher binding affinity of the DMSO towards the metal centre, which blocks the substrate–catalyst interaction is envisaged to be the reason for decreased activity in DMSO.[55] The pH of the catalytic reaction in methanol was found to be 7.2 at RT (the pH of the reaction mixture was measured using a digital pH meter; before each reading the instrument was calibrated using an acid base and neutral buffer). Since the pH of the reaction medium is known to play key role in the catechol oxidase activity,[54] the pH of the catalytic reaction was changed to 10 (by adding 0.1 N NaOH to the reaction mixture) (Entry 5, Table 2) and to 3 (by adding 0.1 N HNO_3 to the reaction mixture) (Entry 6, Table 2). It was evident that, at the basic condition (pH ~ 10, Entry 5, Table 2), the catalytic activity of the system slightly improved, while at the acidic condition (pH ~ 3, Entry 6, Table 2) the catalytic activity decreased significantly. The initial catalytic reaction was carried out at RT (25 °C) (Entry 1, Table 2), in order to examine the effect of temperature, the catalytic reaction was carried out at a higher temperature (*i.e.*, 50 °C) (Entry 7, Table 2). Indeed, at the high temperature, the reaction rate was found to nearly double its value, indicating the positive influence of the temperature on the catalytic reaction. Since all the catalytic reactions were conducted in open air, the atmospheric oxygen is envisaged to be captured and utilized by the catalyst in the current oxidation reaction.[56] Therefore, increase in the oxygen concentration is expected to benefit the reaction. Certainly, when the catalytic reaction was conducted in high oxygen atmosphere (by purging oxygen into reaction mixture, till saturation), noticeable increase in the catalytic activity was observed (Entry 8, Table 2). Fig. 8 shows the UV-vis spectra of the catalytic reactions of catalyst **C1**, (a) under ambient conditions (as Entry 1, Table 2); (b) under high O_2 concentration conditions (as Entry 8, Table 2). Fig. 9 shows the

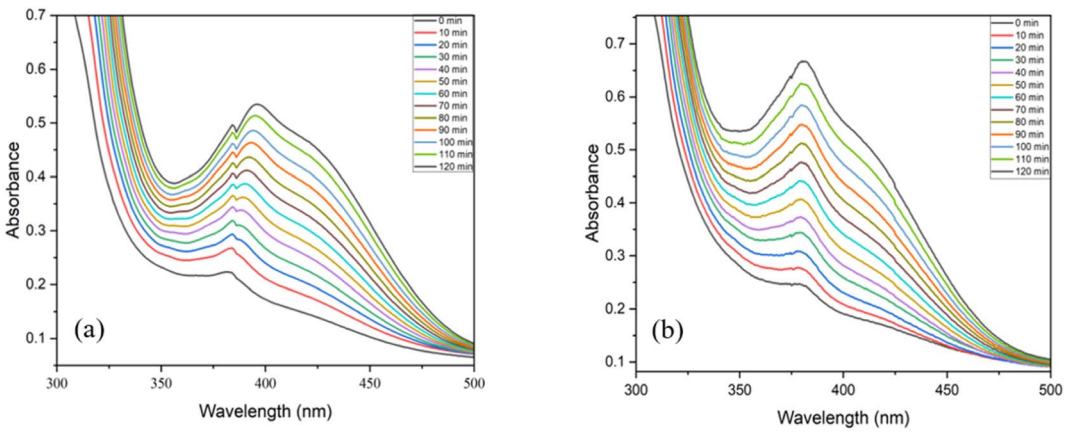

Fig. 8 UV-visible spectra of reaction mixture of **C1** recorded at the time interval of 10 min, (a) under ambient conditions, (b) under high O_2 concentration conditions.

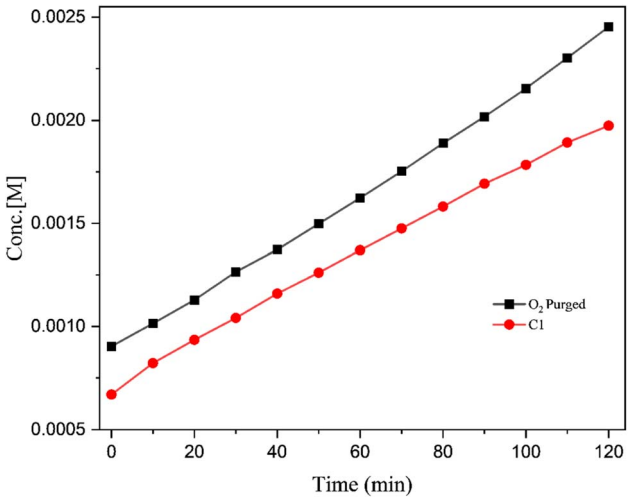

Fig. 9 Plots of concentration of product (DTBQ) concentration *vs.* time for the catalytic reactions conducted at ambient conditions and higher O_2 concentration.

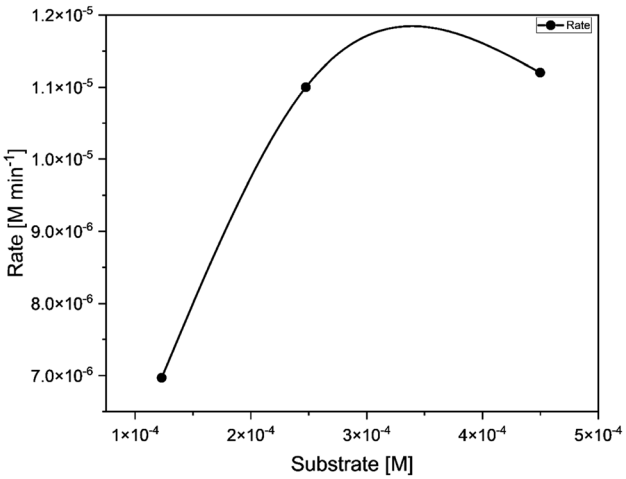

Fig. 11 Concentration of substrate [M] (50, 100, 200) *vs.* rate of the reaction [M min^{-1}] for catalyst **C1**.

plots of change in the product (DTBQ) concentration with respect to time, under ambient condition and under high O_2 concentration.

The oxidation of DTBC by molecular oxygen is expected to yield hydrogen peroxide as a byproduct. The production of hydrogen peroxide in the current reaction was qualitatively analysed by iodine liberation test. The catalytic mixture with a 1 : 10 catalyst: substrate ratio was used for the investigation. The formation of I_3^- was detected by UV-Vis spectral analysis of the reaction mixture (Fig. 10).[9]

The catalyst **C1** was tested with different ratios of 3,5-di-*tert*-butylcatechol (1 : 50, 1 : 100, 1 : 150). The concentration *versus* observed rate plot shows a typical hyperbolic curve (Fig. 11), which is in line with the Michaelis Menten kinetic model. It indicates that the rate of reaction increases with the increase in substrate concentration.[57] The kinetic parameters of the catalytic reaction obtained from the Lineweaver Burk plot are provided in Table 3. This reaction exhibited K_{cat} value of 400 h^{-1} indicating its high potency. K_{cat} values of some of the model compounds containing copper,[58] cobalt,[59] zinc,[60] manganese[61,62] and uranyl[9] centers are listed in Table S9 (ESI†) for comparison.

The EPR spectrum of catalyst **C1** in 5 equivalent 3,5 DTBC in methanol at exhibited a distinct peak at g_{iso} 1.99 and B ~ 326 mT (Fig. 12). This peak indicates the formation of organic radical intermediate during the oxidation of 3,5 DTBC to 3,5 DTBQ.[9] The absence of any additional peaks in the spectrum suggests that catalyst **C1** exhibits diamagnetic characteristics.

Table 3 Kinetic parameters obtained from Lineweaver Burk plot

Complex	V_{max} (M h^{-1})	K_M (M)	K_{cat} (h^{-1})	K_{cat}/K_M
C1	9.7×10^{-4}	1.6×10^{-4}	4.0×10^{2}	4.12×10^{5}

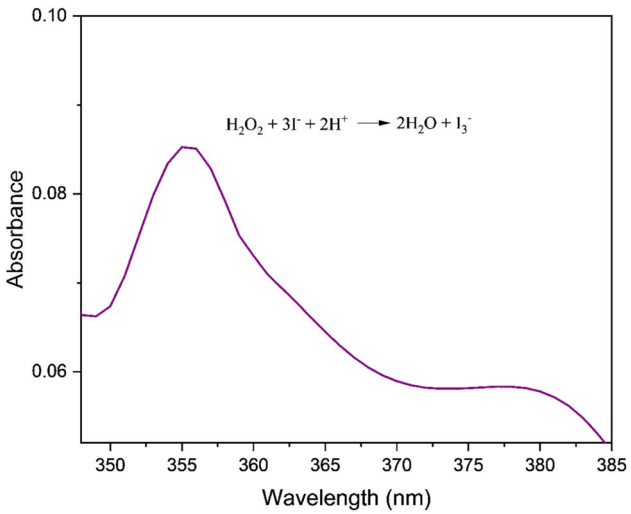

Fig. 10 UV-visible spectrum of the reaction mixture depicting absorption peak corresponding to I_3^- (λ = 353 nm).

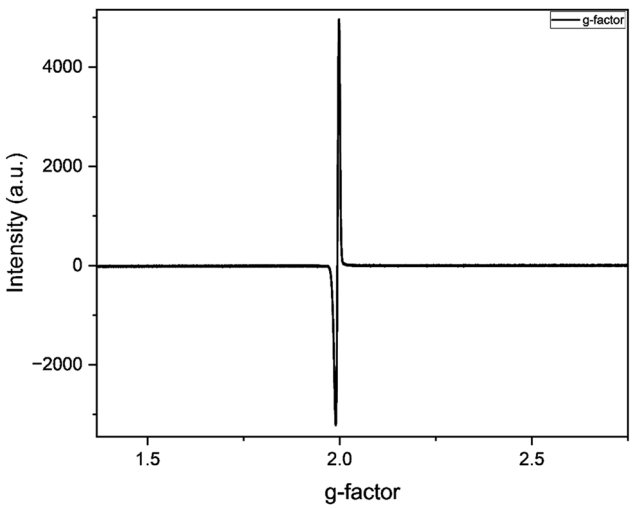

Fig. 12 EPR spectrum of **C1** and 3,5 DTBC reaction mixture (1 : 5) in methanol at 25 °C.

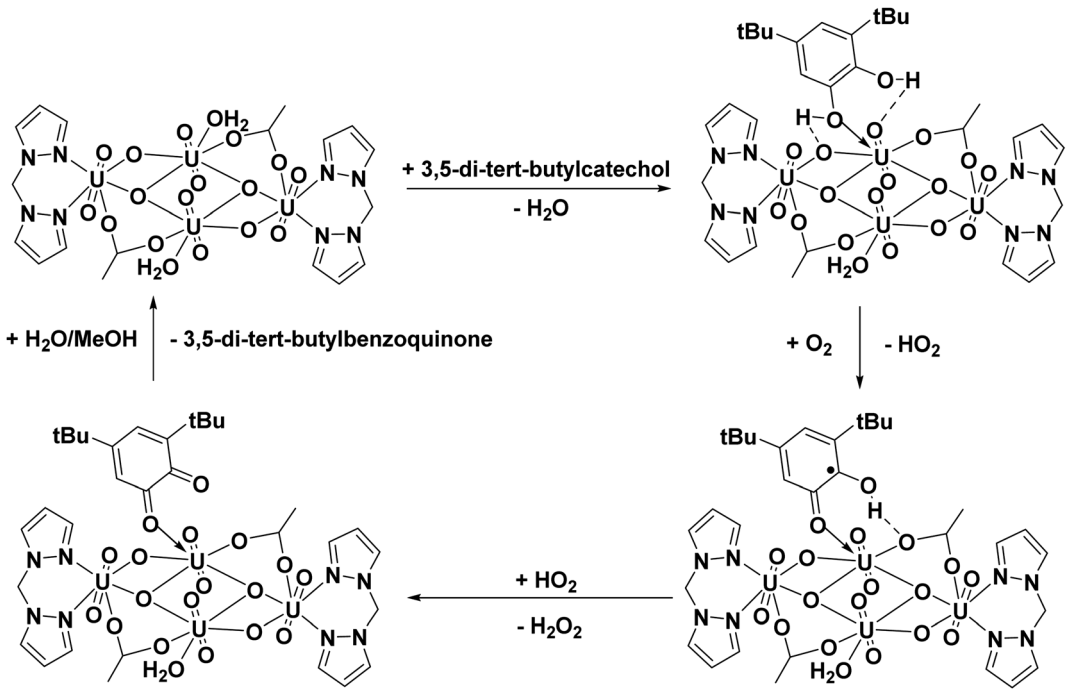

Fig. 13 Proposed catalytic cycle for the oxidation of 3,5-di-*tert*-butyl catechol to 3,5-di-*tert*-butyl benzoquinone.

Proposed catalytic cycle for oxidation of 3,5-di-*tert*-butyl catechol

Based on the experimental observations and previous studies,[9] a plausible mechanistic cycle was established for the catechol oxidase reaction. In the first step, the phenolic OH groups of the catechol model compound (3,5-di-*tert*-butyl catechol) interact with the uranyl center *via* coordination and hydrogen bonding interactions. The next step of the catalytic cycle involves elimination of the H atom from the O-coordinated hydroxyl of the substrate. The substrate further undergoes oxidation in presence of molecular oxygen resulting in the formation of 3,5-di-*tert*-butyl *ortho*-benzosemiquinone (3,5-DTBSQ) and hydroperoxyl radical. The final step of the catalytic cycle involves the abstraction of hydrogen atom from phenolic –OH by hydroperoxyl radical forming hydrogen peroxide and the oxidation of 3,5 DTBSQ to form the product 3,5-di-*tert*-butyl benzoquinone followed by regeneration of the catalyst. The catalytic pathway is depicted in Fig. 13.

Phenoxazinone synthase activity

We analysed the phenoxazinone synthase activity for the complexes **C1** and **C2** using 2-aminophenol as a substrate under aerobic conditions at 25 °C, using deionised water–methanol as the solvent for all the reactions. We analysed the reactions by measuring the increase in the absorbance band at 425 nm, the characteristic λ_{max} for the phenoxazinone chromophore with respect to time (Fig. 14). The rates are calculated from the slope of concentrations *vs.* time graphs (Fig. 15). The calculated

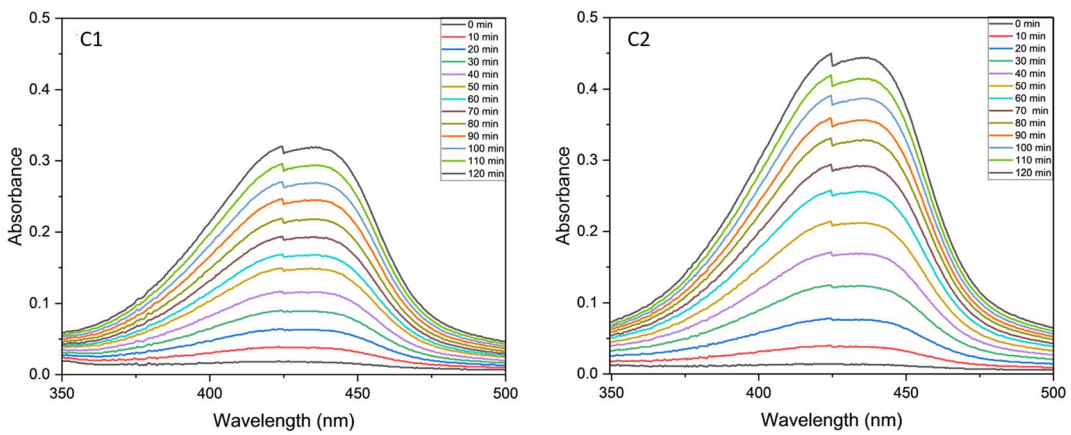

Fig. 14 UV-visible spectra of catalytic mixture of **C1** and **C2** recorded at the time interval of 10 min in a 1 : 50 catalyst to substrate ratio.

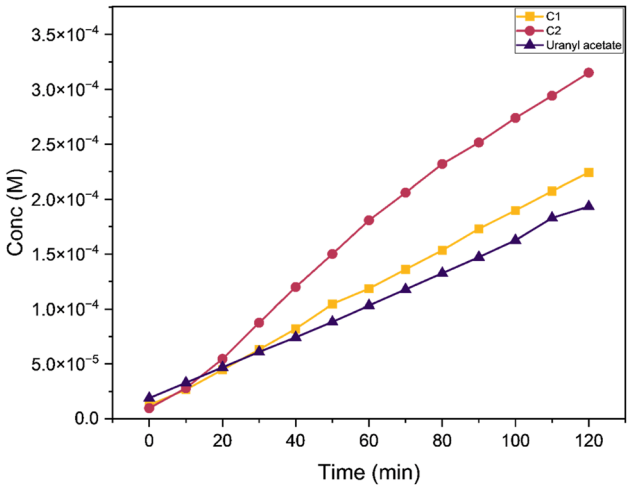

Fig. 15 Conc. (M) *vs.* time (min) graph comparing the change in concentration of the product formed with **C1**, **C2** and uranyl acetate as the reaction progress w.r.t. time at a catalyst to substrate ratio of 1 : 50.

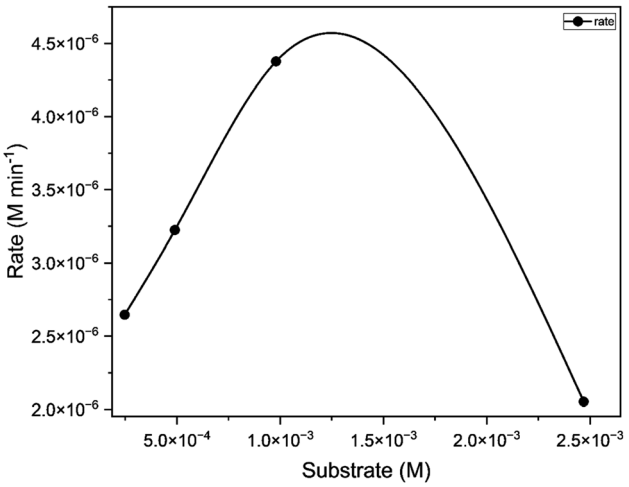

Fig. 16 Concentration of substrate [M] (50, 100, 200, 500) *vs.* rate of the reaction [M min $^{-1}$] for catalyst **C2**.

average rate values are provided in Table 4. The complex **C2** showed faster oxidative dimerization of 2-aminophenol (Entry 2, Table 4) compared to **C1** (Entry 1, Table 4) and bare uranyl acetate (Entry 3, Table 4). The Michaelis-Menton kinetic model (Fig. 16) confirms that, these reactions follow first order kinetics and the corresponding kinetic parameters calculated from Lineweaver Burk plot are listed in the Table 5. Further, the effect of solvent on the oxidation of 2-aminophenol was determined. When the reaction media was changed to an aprotic solvent, DMSO, the reaction rate was found to decrease significantly (Entry 4, Table 4) indicating the need of protic solvent media for the progression of this reaction.[63,64] The impact of pH on the oxidation of 2-aminophenol was investigated by performing the reaction under both acidic and basic conditions. The catalytic conversion of phenoxazinone was substantially decreased when the reaction is carried out under acidic conditions with a pH of 3 (Entry 7 Table 4). Under alkaline conditions with a pH of 10, the reaction rate showed a slight increase (Entry 6 Table 4). This could be attributed to the formation of a more stable complex-substrate adduct, which is favoured at basic pH levels.[65] Several biomimicking catalysts were reported for 2-aminophenol oxidation using transition metals such as copper,[58,65–69] cobalt,[70,71] zinc,[68] and nickel.[68] To best of our knowledge, this is the first uranyl-based catalyst used for 2-aminophenol oxidation. The catalytic efficiency of these metal complexes is compared in a tabular form provided in the ESI (Table S10†).

Table 5 Kinetic parameters obtained from Lineweaver Burk plot

Complex	V_{max} (M h^{-1})	K_M (M)	K_{cat} (h^{-1})	K_{cat}/K_M
C2	3.2×10^{-4}	2.7×10^{-4}	6.6×10^{1}	2.44×10^{5}

Reaction pathway for the oxidation of 2-aminophenol

The mechanism of uranyl catalyzed phenoxazinone synthase reaction is expected to follow the similar path as that of the catechol oxidase reaction described above. In the proposed mechanism for phenoxazinone synthase activity, the initial step of the reaction involves the interaction of 2-aminophenol with the removal of water molecules. The –OH and –NH_2 groups of the substrate form coordinative and the hydrogen bonding interaction with the uranyl center. Further the substrate undergoes oxidation in the presence of O_2 forming 6-iminocyclohexa-2,4-diene-1-one and hydrogen peroxide, regenerating the catalyst. Then, the highly electrophilic 6-iminocyclohexa-2,4-diene-1-one couples with another 2-aminophenol to form 2-amino-4-((2-hydroxyphenyl)amino)phenol (A).

Table 4 Average rate of catalytic reactions (catalyst : substrate (1 : 50)) determined with the help of UV-visible spectral analysis

Sl. no.	Condition	Solvent	Catalyst used	Average rate (M min^{-1})
1	25 °C	Water : MeOH	**C1**	1.79×10^{-6}
2	25 °C	Water : MeOH	**C2**	2.65×10^{-6}
3	25 °C	Water : MeOH	Uranyl acetate	1.51×10^{-6}
4	25 °C	DMSO	**C2**	Trace
5[a]	25 °C	Water : MeOH	**C2**	3.22×10^{-6}
6[a]	25 °C pH 10	Water : MeOH	**C2**	3.41×10^{-6}
7[a]	25 °C pH 3	Water : MeOH	**C2**	Trace

[a] Represents the average rate obtained in a catalyst to substrate ratio of 1 : 100.

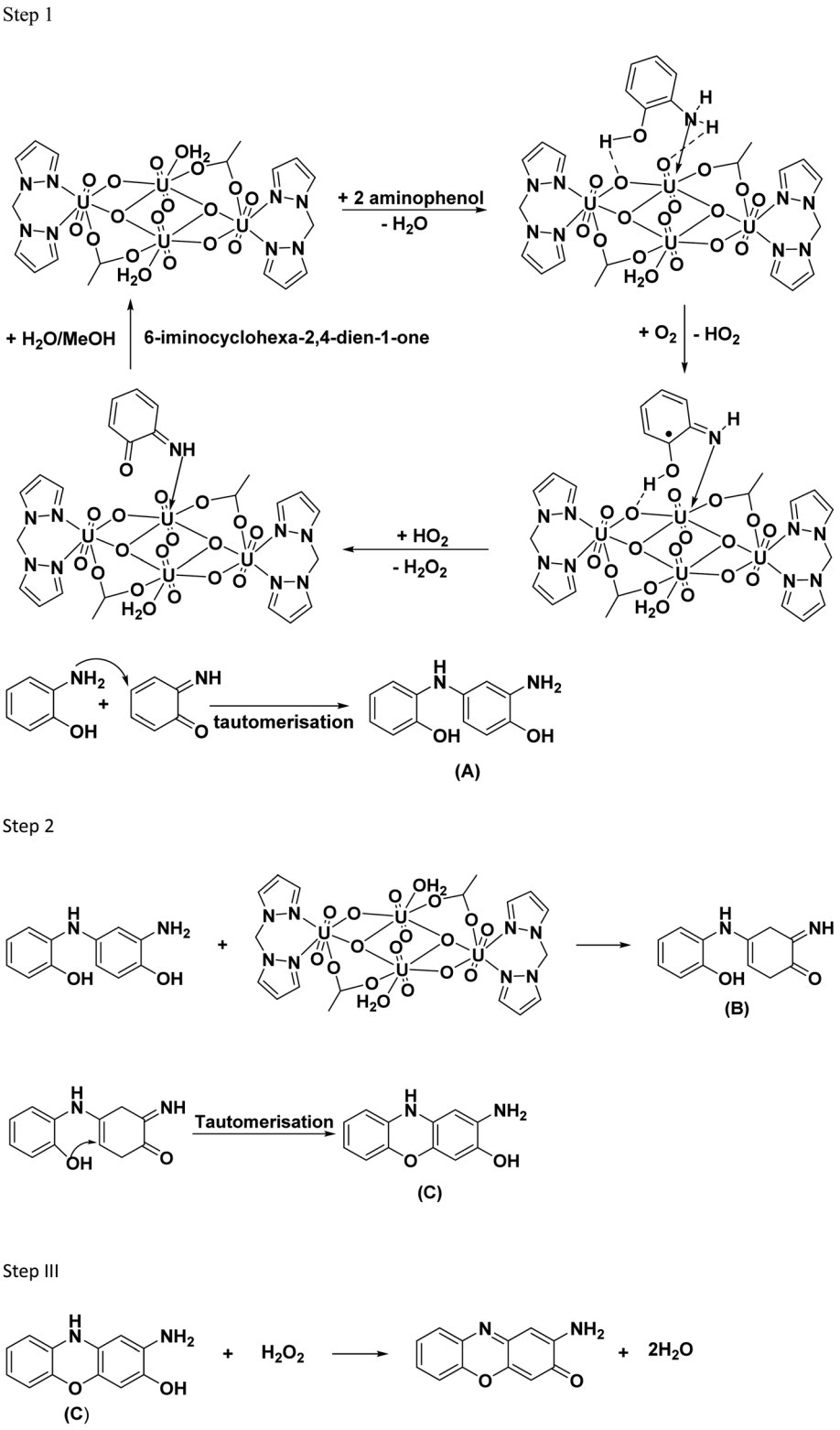

Fig. 17 Proposed reaction pathway for oxidation 2-aminophenol to 2-amino-phenoxazine-3-one using **C1** catalyst.

In step 2, the product A interacts with the catalyst in a similar reaction pathway as step 1, forming the product, 4-((2-hydroxyphenyl)amino)-6-iminocyclohex-3-en-1-one (B). The formed product B undergoes tautomerisation to form product, 2-amino-10*H*-phenoxazin-3-ol (C) and H_2O_2, which is then followed by the catalyst's regeneration. In step 3, the hydrogen peroxide produced in the reaction, oxidizes the product C, leading to the formation of 2-amino-phenoxazine-3-one.[9,65] The reaction pathway is shown in Fig. 17.

Interaction studies of complexes with BSA protein: UV-Vis spectral analysis

Protein interaction studies with the bovine serum albumin and the complexes **C1** and **C2** were monitored using a UV-Vis spectrophotometer.[72] Tris–base HCl was used as a buffer to maintain a pH of 6.94. Protein alone showed absorption at a wavelength in the range of 260 to 290 nm, which is attributed to the n–π* transitions corresponding to the tryptophan and tyrosine amino acids. The complexes **C1** and **C2** at different concentrations (2, 4, 8, 12, 16 and 20 μM) were used for the interaction studies (Fig. 18). In all the mixtures, the characteristic BSA absorption peak at λ_{max} of 280 nm remained unaffected indicating that the microenvironment of the protein chromophore is intact even after binding to the uranyl complex.[73] However, the absorption spectra intensified as the metal ion concentrations increased from 2 to 20 μM. These hyperchromic shifts observed during the interaction studies are mostly due to the metal ion interaction with the tryptophan residue present on the BSA protein's surface.[74,75] The binding constant (K) values for both the complexes were calculated using the intercept to slope ratio (data provided in ESI†).[74] The binding constant for the complex **C1** was determined to be 1.07×10^4 and for complex **C2**, 4.6×10^3, indicating that, complex **C1** binds strongly to the BSA protein than the complex **C2**. Overall, these values indicate the moderate binding ability of the complexes with the protein.[74]

Interaction studies of complexes with BSA protein: fluorescence analysis

The fluorescence studies were utilised to investigate the interaction between the BSA protein and the uranyl complexes **C1** and **C2** in Tris–HCl buffer medium with a pH of 6.94. In these studies, the protein was excited at 296 nm (*i.e.*, tryptophan residues were excited) and the change in the fluorescence was analysed at different concentrations of the complexes **C1** and **C2** by monitoring the emission peak 336 nm for the BSA protein. It was observed that, the fluorescence intensity of BSA with **C1** metal complexes decreases upon increasing the metal complex concentration (Fig. 19). The decrease in intensity was ascribed to the tryptophan quenching mechanism. The Stern–Volmer plot was used to calculate the protein binding efficiency (K_{sv}) of the metal complexes,[73] the K_{sv} value for the complex **C1** is found to be 2.06×10^4. Interestingly, in the case of complex **C2**, increase in the complex concentration resulted into increase in the intensity of the peak, however the binding efficiency is found to be of the same order (*i.e.*, $K_{sv} = 3.6 \times 10^4$).

In vitro cytotoxicity studies

The cytotoxicity assessment of the **C1** and **C2** complexes on the MDA-MB-231 (breast cancer) and A549 (lung cancer) cell lines was performed. In the case of breast cancer cell line, MDA-MB-

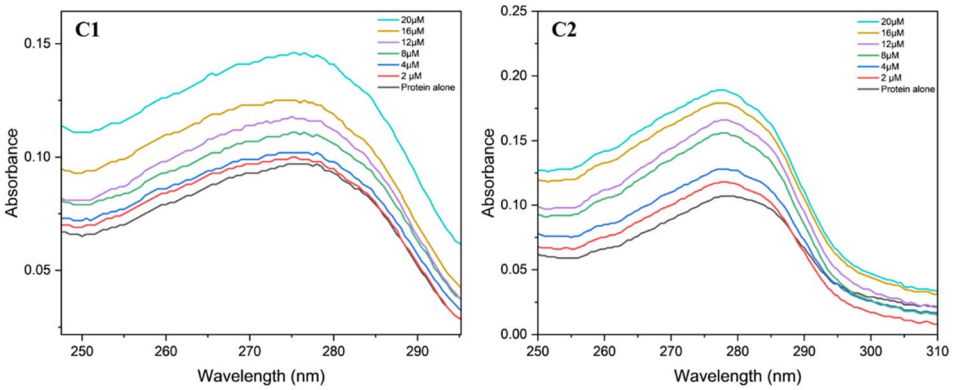

Fig. 18 Absorption spectra BSA protein (2.5 μM) with complexes **C1** and **C2** at different concentrations (2, 4, 8, 12, 16, 20) in μM solutions.

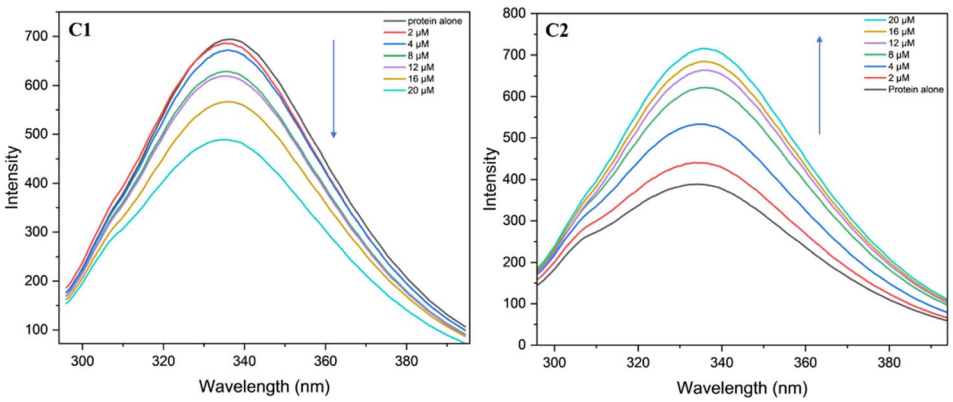

Fig. 19 Fluorescence spectra BSA protein (2.5 μM) with complexes **C1** and **C2** at different concentrations (2, 4, 8, 12, 16, 20) in μM solutions.

Table 6 IC_{50} value of the metal complexes for MDA-MB-231 and A549

Sample name	MDAMB-231 cell line IC_{50} (in μg ml^{-1}) 24 h	A549 cell line IC_{50} (in μg ml^{-1}) 24 h
C1	32.68	24.77
C2	27.66	30.91
Cis-platin	7.87	11.59

231, the compound **C2** was found to exhibit better cytotoxic activity compared to **C1**. On the other hand, studies on A549 lung cancer cells revealed that compound **C1** is more cytotoxic to lung cancer cell lines than the compound **C2**. The corresponding IC_{50} values are provided in Table 6. The graphs showing the cell line viability (%) *vs.* concentration (μg mL^{-1}) are displayed as Fig. 20. From the studies, it is evident that as concentration of uranyl complexes increases, resulting in a decrease in cell viability percentage. Microscope images of MDAMB-231 cell line after treating with two different dosages of complexes **C2**, along with the standard cisplatin and control is depicted in Fig. 21. Similarly, Fig. 22 displays the microscopic images of the A549 cell line with two different doses of **C1** along with cisplatin and untreated cell line. The bis(pyrazolyl) methane and its derivatives show significantly greater IC_{50} values when compared to their corresponding metal complexes or have no anti-cancer efficiency against different cell lines, indicating reduced efficiency and lowered inhibitory activity as an anti-cancer agent.[76–78] In the case of uranyl salts the amount is subsequentially high (ranging from 100 to 250 μM) to inhibit a cancer cell growth.[79]

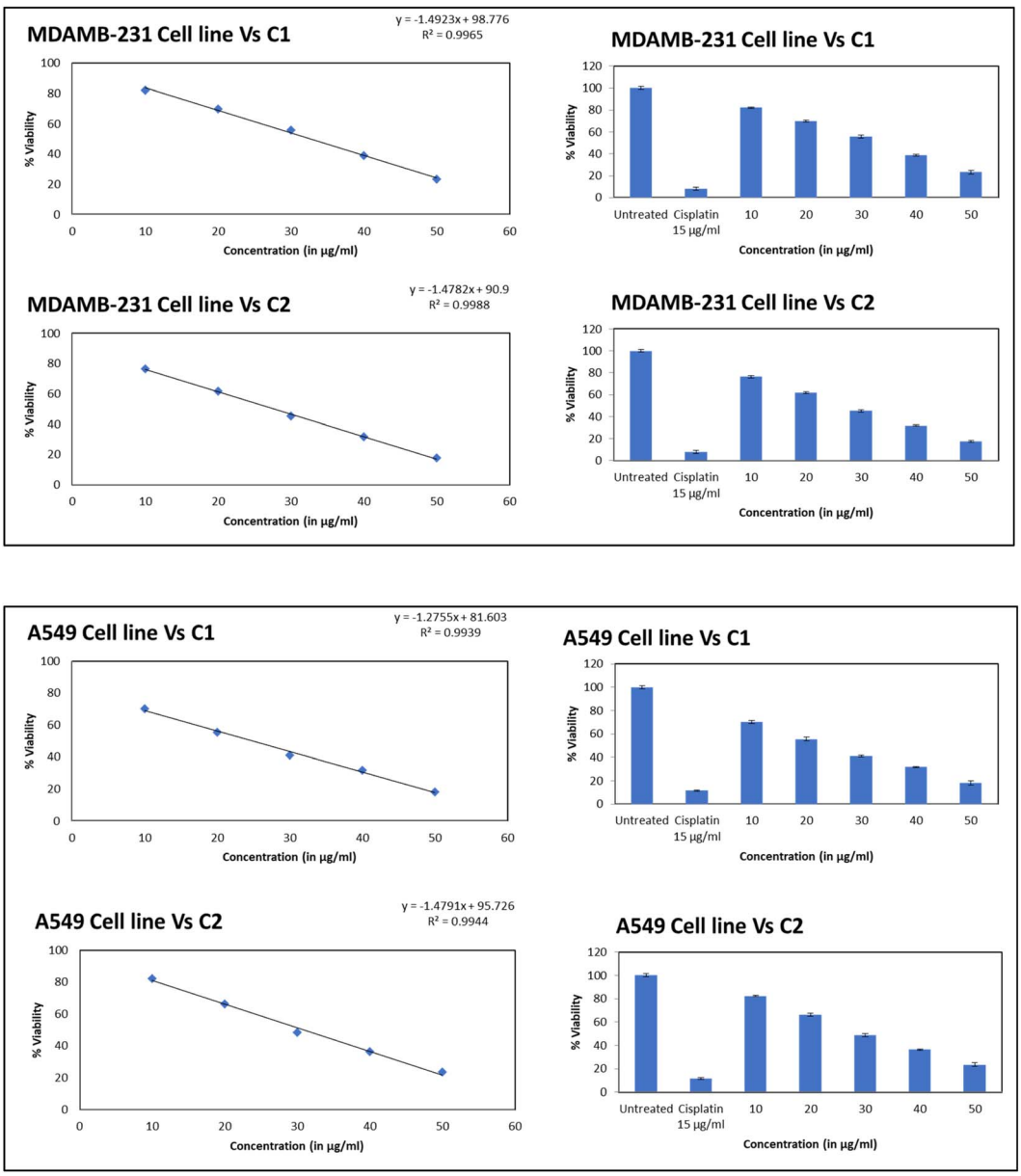

Fig. 20 The graph showing the cell line viability (%) *vs.* concentration (μg mL^{-1}). Top – compound **C1**, bottom – compound **C2**.

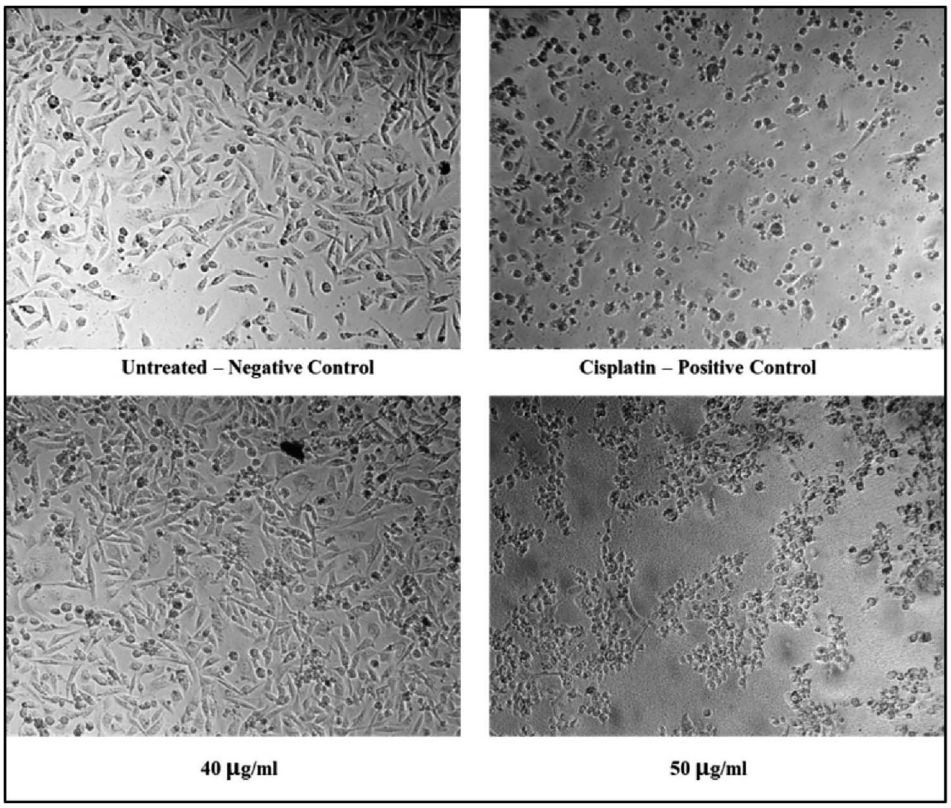

Fig. 21 Microscopic images of MDAMB-231 cell lines treated with 40 and 50 µg mL^{-1} of **C2** in comparison with cisplatin and control.

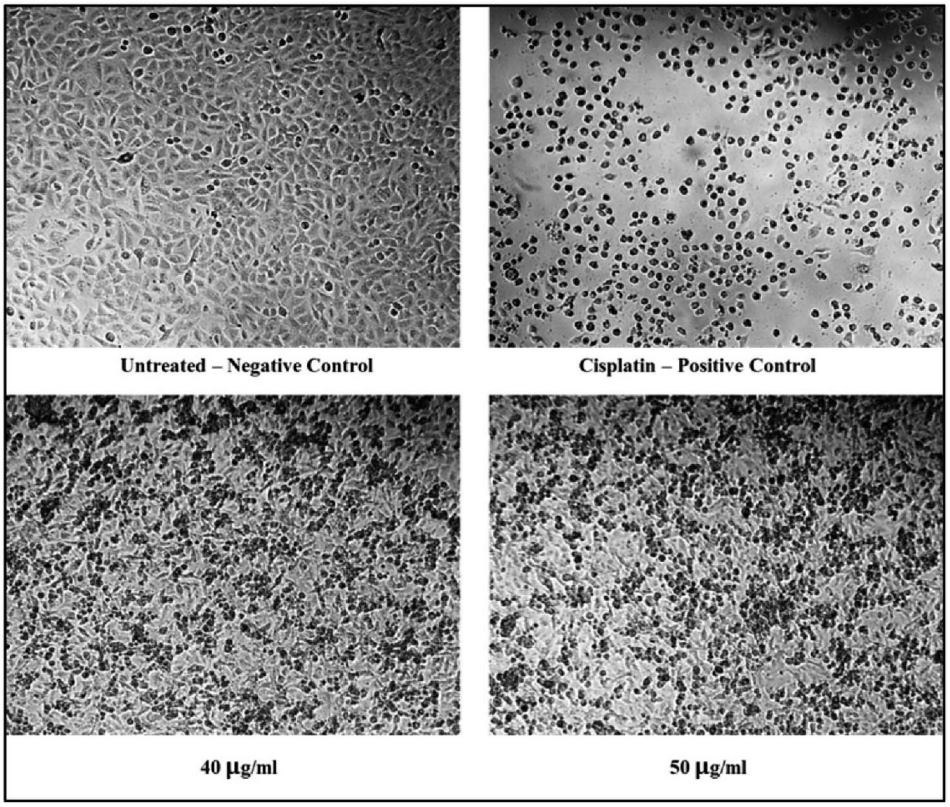

Fig. 22 Microscopic images of A549 cell lines treated with 40 and 50 µg mL^{-1} of **C1** in comparison with cisplatin and control.

Conclusion

Two uranyl complexes, **C1** and **C2**, supported by bis(pyrazolyl) methane ligands, were synthesised and characterised using various spectro-analytical techniques. The structural studies of complex **C1** were conducted using the crystal, which showed a space group of *P*21/*c*. Fluorescence studies were conducted on the complexes, and it was found that the complex synthesised with the ligand containing an electron-donating group exhibited a high fluorescence intensity. The mass spectrum and thermal studies were performed to analyse the chemical structure and temperature stability of the complex, respectively. These catalysts were found to be excellent bio-imitators for the enzyme's catechol oxidase and phenoxazinone synthase in the in the presence of atmospheric air. Complex **C1** has a catalytic efficiency of 4.12×10^5 for the conversion of catechol to quinone, and complex **C2** found to have a catalytic efficiency of 2.44×10^5 for the oxidation of 2-aminophenol in the presence of atmospheric air. The complex **C1** showed better binding ability with the BSA protien, as revealed by the UV-Vis and fluorescence spectroscopyic studies. The anti-cancer studies were conducted for both complexes with two cell lines (breast cancer cell and lung cancer cell). The complex **C1** exhibited an IC_{50} value of 24.77 for the lung cancer cell line, and the complex **C2** showed an IC_{50} value of 27.66 for the breast cancer cells.

Data availability

The data supporting this article have been included as part of the ESI.†

Conflicts of interest

There are no conflicts to declare.

Acknowledgements

NS thanks Amrita Vishwa Vidyapeetham for providing the PhD fellowship. NVK thanks Science and Engineering Research Board (SERB) India for the TARE grant (TAR/2018/000881) and Amrita Vishwa Vidyapeetham for the support. AP thanks Manipal Academy of Higher Education (MAHE), Manipal. Single Crystal XRD Facility and NMR Facility – VIT, Vellore is acknowledged for the aid in the analysis.

References

1 F. Shaki, E. Zamani, A. Arjmand and J. Pourahmad, *Iran. J. Pharm. Res.*, 2019, **18**, 90.
2 O. C. Lind, J. Tschiersch and B. Salbu, *J. Environ. Radioact.*, 2020, **211**, 106077.
3 W. Chen, H.-M. Yuan, J.-Y. Wang, Z.-Y. Liu, J.-J. Xu, M. Yang and J.-S. Chen, *J. Am. Chem. Soc.*, 2003, **125**, 9266–9267.
4 P. Thuéry, C. Villiers, J. Jaud, M. Ephritikhine and B. Masci, *J. Am. Chem. Soc.*, 2004, **126**, 6838–6839.
5 K. Darzinezhad, M. M. Amini, E. Mohajerani, M. Armaghan, T. O. Knedel, A. Abareghi and C. Janiak, *Dalton Trans.*, 2019, **48**, 3695–3703.
6 K. Darzinezhad, M. M. Amini, M. Janghouri, E. Mohajerani, M. R. Fathollahi, Z. Jamshidi and C. Janiak, *Inorg. Chem.*, 2020, **59**, 17028–17037.
7 L. Ding, J. Leduc, T. Fischer, S. Mathur and Y. Li, *Nanoscale Adv.*, 2020, **2**, 2478–2484.
8 S. Ghosh, A. K. Srivastava, R. Govu, U. Pal and S. Pal, *Inorg. Chem.*, 2019, **58**, 14410–14419.
9 S. Ghosh, A. K. Srivastava, M. Sharma and S. Pal, *ChemistrySelect*, 2022, **7**, e202200293.
10 Z. Zhou, X.-B. Li, Z. Huang, Q.-Y. Wu, J.-X. Wang, Z.-H. Zhang, J. Yu, L. Mei, F. Ma and K. Hu, *Inorg. Chem. Front*, 2024, **11**, 6493–6501.
11 N. Behera and S. Sethi, *Eur. J. Inorg. Chem.*, 2021, **2021**, 95–111.
12 A. A. Sharfalddin, A.-H. Emwas, M. Jaremko and M. A. Hussien, *PLoS One*, 2021, **16**, e0256186.
13 A. M. Khedr and F. A. Saad, *Turk. J. Chem.*, 2015, **39**, 267–280.
14 M. Gaber, H. A. El-Ghamry, S. K. Fathalla and M. A. Mansour, *Mater. Sci. Eng., C*, 2018, **83**, 78–89.
15 Z. Asadi, M. Asadi, F. Dehghani Firuzabadi, R. Yousefi and M. Jamshidi, *J. Iran. Chem. Soc.*, 2014, **11**, 423–429.
16 M. Y. Zhao, R. J. Ma, Y. N. Chen, H. X. Zhang, K. Kong, H. Bin Chu, F. Y. Zhao and Y. L. Zhao, *Appl. Mech. Mater.*, 2013, **271**, 55–59.
17 L. Götzke, G. Schaper, J. März, P. Kaden, N. Huittinen, T. Stumpf, K. K. K. Kammerlander, E. Brunner, P. Hahn and A. Mehnert, *Coord. Chem. Rev.*, 2019, **386**, 267–309.
18 Y.-W. Lin, *Biomolecules*, 2020, **10**, 457.
19 S. Trofimenko, *J. Am. Chem. Soc.*, 1970, **92**, 5118–5126.
20 S. Swathy, H. Chandran, G. Reshma, S. Nakul, M. Kumar, M. A. Krishnan, N. V Kulkarni, D. Senthurpandi, S. S. Contractor and S. B. Arakera, *J. Mol. Struct.*, 2022, **1251**, 132018.
21 N. V Kulkarni and V. K. Revankar, *J. Coord. Chem.*, 2011, **64**, 725–741.
22 M. Roy, A. Adhikary, A. K. Mondal and R. Mondal, *ACS Omega*, 2018, **3**, 15315–15324.
23 N. V. Kulkarni, C. Dash, N. B. Jayaratna, S. G. Ridlen, S. Karbalaei Khani, A. Das, X. Kou, M. Yousufuddin, T. R. Cundari and H. V. R. Dias, *Inorg. Chem.*, 2015, **54**, 11043–11045.
24 V. Hegde, C. O. Sreekala, N. V Kulkarni and J. Mathew, *J. Photochem. Photobiol., A*, 2024, **449**, 115389.
25 V. Hegde, C. O. Sreekala, N. V Kulkarni, D. Senthurpandi and J. Mathew, *J. Mol. Struct.*, 2022, **1266**, 133512.
26 G. M. Sheldrick, *Acta Crystallogr.*, 2015, **C71**, 3–8.
27 G. M. Sheldrick, *Acta Crystallogr.*, 2008, **A64**, 112–122.
28 L. J. Farrugia, *J. Appl. Crystallogr.*, 2012, **45**, 849–854.
29 **https://www.ccdc.cam.ac.uk/Community/csd-community/Free-Mercury/**.
30 S. K. Dey and A. Mukherjee, *Coord. Chem. Rev.*, 2016, **310**, 80–115.
31 S. K. Dey and A. Mukherjee, *New J. Chem.*, 2014, **38**, 4985–4995.

32 M. El Boutaybi, N. Bouroumane, M. Azzouzi, M. Aaddouz, S. Bacroume, M. El Miz, R. Touzani, Z. Bahari, A. Zarrouk and A. El-Marghany, *Crystals (Basel)*, 2023, **13**, 155.
33 D. Gerlier and N. Thomasset, *J. Immunol. Methods*, 1986, **94**, 57–63.
34 M. C. Alley, D. A. Scudiere, A. Monks, M. Czerwinski, R. Shoemaker and M. R. Boyd, *Proc. Am. Assoc. Cancer Res.*, 1986, **27**, 389.
35 D. Gerlier and N. Thomasset, *J. Immunol. Methods*, 1986, **94**, 57–63.
36 *MTT Cell Proliferation Assay Instruction Guide*, ATCC, VA, USA, **https://www.atcc.org**.
37 G. Reshma, S. Nakul, P. M. Mahitha, N. V Kulkarni, D. Senthurpandi, S. S. Yamijala, W. W. Brennessel and W. D. Jones, *J. Mol. Struct.*, 2022, **1251**, 132005.
38 H. B. Howsaui, A. S. Basaleh, M. H. Abdellattif, W. M. I. Hassan and M. A. Hussien, *Biomolecules*, 2021, **11**, 1138.
39 G. L. Caldow, A. B. Van Cleave and R. L. Eager, *Can. J. Chem.*, 1960, **38**, 772–782.
40 B. S. Satyanarayana, *Proc. Natl. Acad. Sci., India, Sect. A*, 1942, **15**, 414–416.
41 M. Dembowski, V. Bernales, J. Qiu, S. Hickam, G. Gaspar, L. Gagliardi and P. C. Burns, *Inorg. Chem.*, 2017, **56**, 1574–1580.
42 V. Krishnakumar, N. Jayamani and R. Mathammal, *Spectrochim. Acta, Part A*, 2011, **79**, 1959–1968.
43 A. S. Potapov and A. I. Khlebnikov, *Polyhedron*, 2006, **25**, 2683–2690.
44 G. Feng, K. N. McCabe, S. Wang, L. Maron and C. Zhu, *Chem. Sci.*, 2020, **11**, 7585–7592.
45 E. Badaruddin, Z. Aiyub, Z. Abdullah and S. B. Nasir, *Malays. J. Anal. Sci.*, 2009, **13**, 129–135.
46 Y. Suzuki, M. Yamaji, S. Maki and T. Hirano, *J. Photochem. Photobiol., A*, 2016, **314**, 93–95.
47 R. Agarwal and M. K. Sharma, *Inorg. Chem.*, 2018, **57**, 10984–10992.
48 M. Azam, G. Velmurugan, S. M. Wabaidur, A. Trzesowska-Kruszynska, R. Kruszynski, S. I. Al-Resayes, Z. A. Al-Othman and P. Venuvanalingam, *Sci. Rep.*, 2016, **6**, 32898.
49 P. C. Burns, R. C. Ewing and F. C. Hawthorne, *Can. Mineral.*, 1997, **35**, 1551–1570.
50 A. A. Sharfalddin, A.-H. Emwas, M. Jaremko and M. A. Hussien, *PLoS One*, 2021, **16**, e0256186.
51 I. M. Yanachkova and M. Staevsky, *J. Mater. Sci.*, 1973, **8**, 606–610.
52 A. Sarkar, A. Chakraborty, A. Adhikary, S. Maity, A. Mandal, D. Samanta, P. Ghosh and D. Das, *Dalton Trans.*, 2019, **48**, 14164–14177.
53 M. A. Chrisman, M. J. Goldcamp, A. N. Rhodes and J. Riffle, *J. Chem. Educ.*, 2023, **100**, 893–899.
54 M. Ashafaq, M. Raizada, M. Khalid, M. Shahid, M. Ahmad and Z. A. Siddiqi, *J. Coord. Chem.*, 2018, **71**, 2118–2145.
55 M. Shahid, I. Mantasha, S. Khan, M. Mehtab, O. Yadav, A. Ansari, K. M. A. Qasem, A. Ahmed, M. Saniya and M. N. Akhtar, *J. Mol. Struct.*, 2021, **1244**, 130878.
56 K. Pal, S. Barman and J. Bag, *Chem. Biodivers.*, 2023, **20**, e202201166.
57 D. Mukherjee, P. Nag, A. A. Shteinman, S. R. Vennapusa, U. Mandal and M. Mitra, *RSC Adv.*, 2021, **11**, 22951–22959.
58 S. Reja, D. Sarkar, K. Sarkar, D. Mukherjee, T. K. S. Fayaz, P. Sanphui and R. K. Das, *Inorg. Chim. Acta*, 2024, **560**, 121809.
59 R. R. Tripathy, P. K. Deheri, P. Biswas, S. Jana and S. Sarkar, *J. Mol. Struct.*, 2024, **1312**, 138576.
60 S. Das, A. Sahu, M. Joshi, S. Paul, M. Shit, A. Roy Choudhury and B. Biswas, *ChemistrySelect*, 2018, **3**, 10774–10781.
61 P. Seth, L. K. Das, M. G. B. Drew and A. Ghosh, *Eur. J. Inorg. Chem.*, 2012, **2012**, 2232–2242.
62 M. S. Khan, M. Khalid, M. S. Ahmad, M. Shahid and M. Ahmad, *Res. Chem. Intermed.*, 2020, **46**, 2985–3006.
63 A. Mouadili, D. Mazouzi and R. Touzani, *Iran. J. Chem. Chem. Eng.*, 2023, **42**, 1111–1125.
64 A. Mouadili, A. Attayibat, S. El Kadiri, S. Radi and R. Touzani, *Appl. Catal., A*, 2013, **454**, 93–99.
65 N. Podder and S. Mandal, *New J. Chem.*, 2020, **44**, 12793–12805.
66 S. Mukherjee, S. Roy, S. Mukherjee and B. Biswas, *J. Mol. Struct.*, 2020, **1217**, 128348.
67 M. Garai, D. Dey, H. R. Yadav, A. R. Choudhury, M. Maji and B. Biswas, *ChemistrySelect*, 2017, **2**, 11040–11047.
68 A. Chatterjee, S. Khan and R. Ghosh, *Polyhedron*, 2019, **173**, 114151.
69 W. P. Sohtun, S. Muthuramalingam, M. Sankaralingam, M. Velusamy and R. Mayilmurugan, *J. Inorg. Biochem.*, 2021, **216**, 111313.
70 A. K. Maji, A. Chatterjee, S. Khan, B. K. Ghosh and R. Ghosh, *J. Mol. Struct.*, 2017, **1146**, 821–827.
71 K. Ghosh, K. Harms and S. Chattopadhyay, *ChemistrySelect*, 2017, **2**, 8207–8220.
72 A. Singh, A. Kumar, P. Kumar, T. Bhardwaj, R. Giri and N. Garg, *Future Med. Chem.*, 2021, **13**, 1341–1352.
73 A. Baral, L. Satish, D. P. Das, H. Sahoo and M. K. Ghosh, *New J. Chem.*, 2017, **41**, 8130–8139.
74 H. A. Alhazmi, M. S. Alam, M. Albratty, A. Najmi, A. A. Abdulhaq, R. Hassani, W. Ahsan and A. N. Qramish, *J. Chem.*, 2023, **2023**, 2581653.
75 M. Zhou, Y. Bi, H. Zhou, X. Chen, F. Zhang, Y. Li and X. Qu, *ChemistryOpen*, 2021, **10**, 373–379.
76 C. Di Nicola, F. Marchetti, C. Pettinari, R. Pettinari, F. Brisdelli, M. Crucianelli, C. Lelii and A. Crispini, *Inorg. Chim. Acta*, 2017, **455**, 677–682.
77 P. Seguí, J. J. Aguilera-Correa, E. Domínguez-Jurado, C. M. Sánchez-López, R. Pérez-Tanoira, A. V Ocaña, J. A. Castro-Osma, J. Esteban, A. Marcilla and C. Alonso-Moreno, *Sci. Rep.*, 2021, **11**, 16306.
78 M. Pellei, V. Gandin, L. Marchiò, C. Marzano, L. Bagnarelli and C. Santini, *Molecules*, 2019, **24**, 1761.
79 A. Carmona, V. Malard, E. Avazeri, S. Roudeau, F. Porcaro, E. Paredes, C. Vidaud, C. Bresson and R. Ortega, *Neurotoxicology*, 2018, **68**, 177–188.